Towards the prediction of wall-pressure fluctuations for space launchers using ZDES-based convolutional neural networks

LECLER Simon[*][†]*, WEISS Pierre-Élie* [*] *and DECK Sébastien* [*]
[*]*DAAA, ONERA, Université Paris Saclay*
F-92190 Meudon, France
simon.lecler@onera.fr · pierre-elie.weiss@onera.fr · sebastien.deck@onera.fr
[†]Corresponding author

Abstract

Convolutional neural networks (CNNs) are developed to predict the RMS wall-pressure coefficient and single-point wall-pressure spectra in the separating/reattaching flow region of a space launcher in the transonic regime. Trained on a generic launcher afterbody configuration (NASA model 11 hammerhead), the present models are found to accurately predict the evolution of the aforementioned quantities for the tested launcher geometry. A scaling method is proposed to retrieve correct magnitudes for a given configuration. It is also demonstrated that good performances are achieved with the models using data from RANS simulation as input, paving the way for a drastic reduction in the computational cost for predicting wall-pressure fluctuations around space launchers.

1. Introduction

During transonic flight, launch vehicles can be subjected to unsteady aerodynamic loads related to high-level pressure fluctuations. The induced lateral loads can endanger the payload and the launcher itself. In particular, the unsteady pressure field resulting from the separation followed by reattachement of the flow is highly dependent on the launcher geometry and needs to be assessed for each new configuration.[8] Therefore, the knowledge of the fluctuating wall-pressure field is of major importance for the design of space launchers. Current advanced turbulence modelling methods like hybrid RANS/LES are able to predict the unsteady pressure field for a complex configuration with a given fidelity level.[19,33,34] However, they are still costly in terms of computational time and resources, especially applied to realistic, high Reynolds flows. In the earlier phases of design, surrogate models could help providing insights into the unsteady wall-pressure field, namely the local root-mean-square pressure coefficient and the single-point wall-pressure spectrum. Empirical[5,9,15] and analytical[2,3,16,20] models exist to predict the fluctuating pressure coefficient, single-point power spectra and two-point cross-spectra. However, these models were developed for attached flows and are tuned for specific flow conditions. They are not adapted to compressible, three-dimensional separated flows

This study proposes a data-driven approach, using convolutional neural networks to predict the wall-pressure fluctuations around a space launcher, with mean flow data as input. The objective is to predict the RMS pressure coefficient and power spectra in the separating/reattaching flow regions. Two CNNs (one for each aforementioned quantity) are trained on a generic afterbody configuration. Datasets were built from Zonal Detached Eddy Simulations (ZDES)[10,11] of the training and testing configurations. The first part of this paper is devoted to the description of the test cases and the comparison of the numerical simulations to available experimental results. Then, the machine learning methodology used to build wall-pressure fluctuations models is detailed. Finally, trained models are evaluated in the last section.

2. Test cases: description and validation

Training and testing datasets were built from two numerical simulations of transonic flows around axisymmetric configurations, involving separation and reattachment of the flow. The first configuration was dedicated to the training procedure of the neural networks, the second one beeing used as a testing case. Both cases are computed using Zonal Detached Eddy Simulation (ZDES). Let us be reminded that ZDES is a multiresolution method developed by ONERA[10,11] which covers the full modelling range from RANS to WRLES. This work is mainly based on ZDES mode 2 (2020), a fully automatic model where the model sets dynamically by itself the RANS-LES interface.

2.1 Training case: S3Ch generic afterbody

The S3Ch generic afterbody configuration consists of two adjacent cylinders of diameter $D = 100$ mm and $d = 40$ mm that features a massively separated base flow as classically encountered on space launchers afterbodies. Numerous ZDES computations of this configuration have already been conducted and validated[12, 22, 35, 36] using the experimental data of Deprés et al.[13] and Meliga and Reijasse.[21]

In this work, we used the results of the simulation previously conducted by Pain et al.[22] focusing on the transonic flow regime at a free-stream Mach number $M_\infty = 0.7$. The Reynolds number based on the forebody diameter is $Re_D = 1.2 \times 10^6$, the boundary layer thickness at the edge of the largest cylinder is $\frac{\delta_0}{D} = 0.2$, and the free stream dynamic pressure is $q_\infty = \frac{\gamma}{2} M_\infty^2 P_\infty \approx 24\,815$ Pa. The multiblock structured mesh is composed of 12×10^6 hexaedric cells, with 240 cells in the azimuthal direction. The time step of the simulation is $\Delta t_{CFD} = 2$ µs. More details about the computation can be found in Pain et al.[22] .

An overview of the instantaneous turbulent field and mean organization of the flow is provided in figure 1. The spatial organisation of the coherent structures in the turbulent flow is evidenced in figure 1(a), with an isosurface of the dimensionless Q-criterion ($Q^* = \frac{QD^2}{U_\infty^2}$) coloured by the Mach number, along with iso-contours of the pseudo-schlieren in a cut-off plane and at the wall. This plot shows the presence of an axisymmetric shear layer that grows and impinges the second cylinder, with the presence of vortices of various scales. The time-averaged flow field is represented in figure 1(b) with the dimensionless streamwise velocity field and the dimensionless pressure at the wall. The reattachment region is identified by the mean streamlines, and is characterized by high pressure levels and a plateau in the fluctuating pressure coefficient Cp_{rms} curve. Finally, figure 1(c) displays a log-log axis plot of the normalized premultiplied power spectral density of wall pressure fluctuations ($\frac{fG_{p'}(f)}{\sigma^2}$ where f is the frequency, $G_{p'}$ the PSD and σ is the standard deviation of the fluctuating pressure signal) in the middle of the recirculation zone.
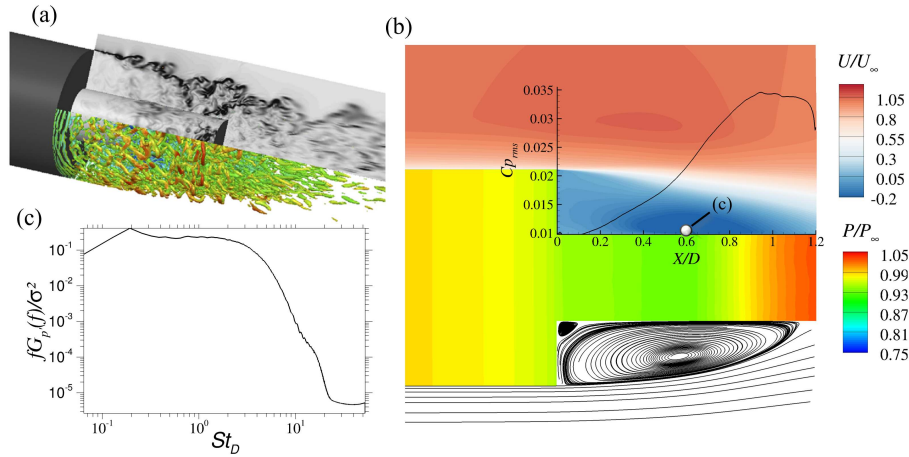

Figure 1: (a) Isosurfaces of the normalized Q-criterion ($Q^* = 50$) coloured by the streamwise velocity and numerical pseudo-schlieren (gray scale) in a cut-off plane and on the skin of the emerging cylinder (taken from Pain et al.[22]). (b) RMS pressure coefficient at the wall of the emerging cylinder and mean organization of the flow with a cut-off plane of the dimensionless streamwise velocity (top), mean streamlines (bottom) and the dimensionless static pressure at the wall. (c) Normalized premultiplied PSD of the pressure at the wall for the streamwise location $x/D = 0.6$.

2.2 Application case: NASA model 11 hammerhead launch vehicle

The test case configuration is the NASA model 11 hammerhead launch vehicle experimentally studied by Coe et Nute [16] and Schuster et al.[26] The geometry is described in figure 2(a). Free-stream conditions are chosen to reproduce the experiment of Schuster et al,[26] also reported by Panda et al.[24] The Mach number equals 0.8, the total pressure and temperature are $P_i = 236255$ Pa and $T_i = 790$ K. The Reynolds number based on the payload diameter ($D = 0.24$ m) is $Re_D = 2.4 \times 10^6$.

The multi-block structured mesh is shown in figure 2(b). The mesh includes 24×10^6 hexaedric cells, including $N_\phi = 240$ points in the azimuthal direction. The grid is built on an O-H topology to avoid any singularity problem near the axis. In the wall-normal direction, the dimensionless first cell size is $\Delta y^+ = 1$ and the early stages of the vorticity thickness development are modelled with 15 points, as advised by Simon et al.[28] The length and diameter of the computational

domain are respectively 246D and 320D, willingly high compared to the reference diameter to avoid any reflections of spurious numerical waves. The first stage has been extended up to the end of the domain.

Numerical sensors are located on every cells in the streamwise direction in the separating/reattaching flow region. For each streamwise location, 4 sensors are regularly distributed in the azimuthal direction. Pressure signal was acquired during 0.3 s of physical time. The time step of the simulation equals 0.2 µs. Sampling is performed every 10 time steps, corresponding to a sampling frequency of 500 kHz.

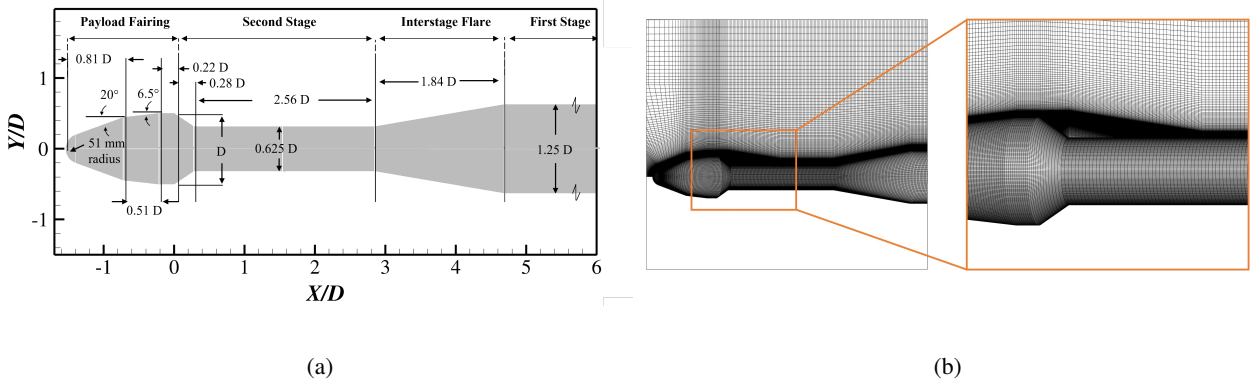(a)   (b)

Figure 2: (a) Sketch of the geometry of the NASA model 11 hammerhead configuration (b) Computational mesh in a streamwise cut-off plane

The salient features of the instantaneous flow are displayed in figure 3, with a plot of an isosurface of the normalized Q-criterion $Q^* = 2$ coloured by the Mach number and a cut-off plane of numerical schlieren. The flow topology is similar to the previous case. Just after separation, one can note the presence of toroidal structures related to the Kevin-Helmholtz instability. The coherent structures grow in size and impinge the wall . Downstream of reattachment, the vortex shedding phenomenon is observed, mainly responsible for the pressure fluctuations along the flare and the first stage.
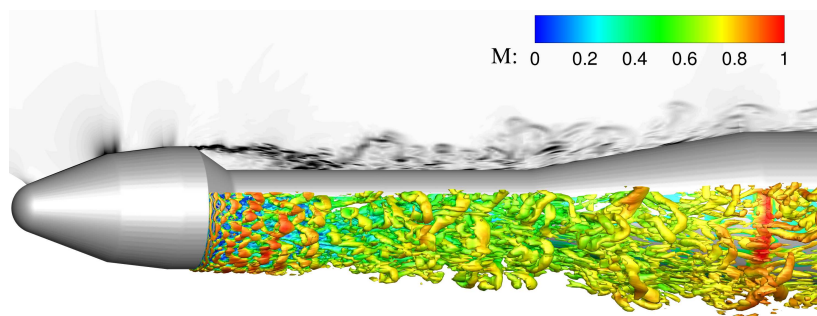

Figure 3: Instantaneous turbulent field of the flow around the NASA model 11 computed by ZDES

The two targeted quantities, namely the RMS pressure coefficient and the dimensionless power spectral density of wall-pressure fluctuations $\frac{U_\infty G'_p(f)}{Dq_\infty^2}$, are plotted in figure 4. The proposed models will be applied in the range $0.37 < \frac{X}{D} < 1.42$, corresponding to the separated and reattachment regions of the flow.

The ZDES computation was validated by comparison with the experimental results of Schuster et al.,[26] Coe and Nute[7] and Panda et al.[24] The computed mean pressure coefficient Cp distribution is plotted in the streamwise direction in figure 5(a). The present ZDES simulation is in very good agreement with both experimental datasets. To compare the Cp_{rms} coefficient with measured data, the simulated pressure signal was filtered according to the experiments. Results are displayed in figure 5(b). Downstream from the separation point, in the region treated with LES, numerical results are in good agreement with experimental data.

3. Methodology

This section is devoted to the description of the prediction process and the methodology used to design, train and apply the present data-driven models.
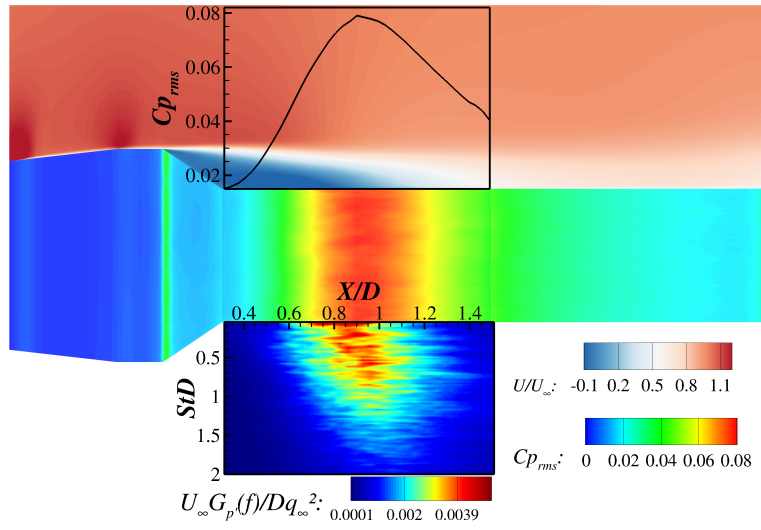
Figure 4: Visualization of the fluctuating quantities of interest: RMS pressure coefficient (top) and spectral map of the dimensionless premultiplied power spectral density $U_\infty G'_p(f)/q^2_\infty D$ (bottom) in the domain of interest defined by the interval $X/D = [0.37, 1.42]$, along with a cut-off plane of the dimensionless mean streamwise velocity and Cp_{rms} at the wall.
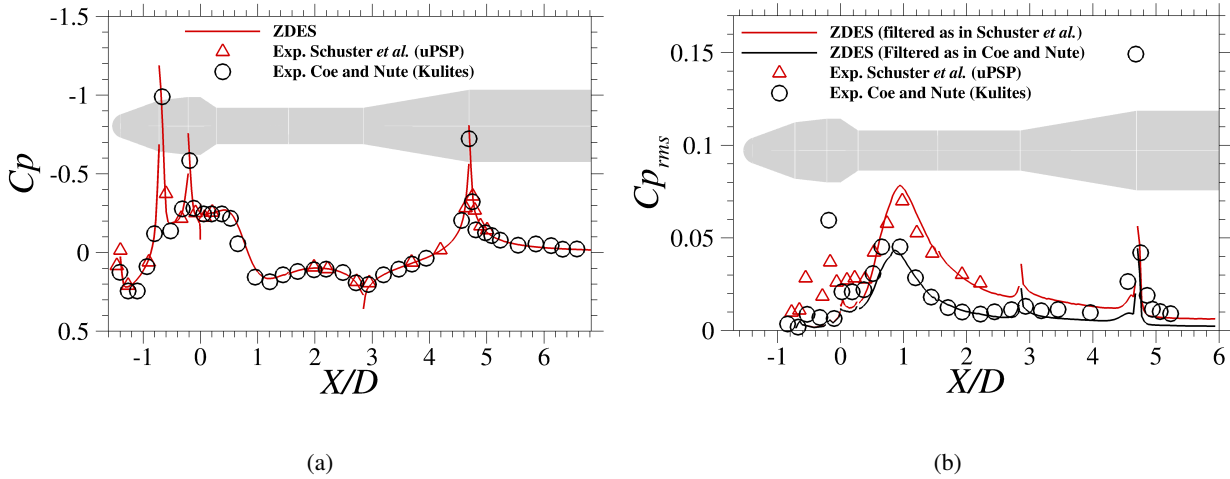

Figure 5: (a) Comparison of measured and computed Cp values (b) Comparison of measured and computed filtered Cp_{rms} values. The values were obtained by integrating the power spectral density of pressure in the band-pass range of 10-800 Hz according to the experiment of Coe and Nute[7] and 0-10 kHz corresponding to the experiment of Schuster et al.[26]

3.1 Prediction strategy

A sketch of the prediction process is presented in figure 6. Two CNNs are trained, for the prediction of Cp_{rms} and the dimensionless pressure spectra, respectively. The machine learning libraries (i.e. scikit-learn,[32] Tensorflow,[1] Keras[6]) used to process data and build the neural networks are mentioned.

A preliminary CFD computation yields the mean flow field used to build the input dataset. A data preprocessing step called standardization consists in standardizing input variables to have 0 mean and unit standard deviation. This is a common and important practice to improve the quality of the training process.[27] The operation is applied to the output training data as well. The Python library scikit-learn[32] is employed to proceed to this preprocessing operation. The resulting input dataset is passed as input to the convolutional neural networks. Both CNNs are implemented and trained using Tensorflow[1] with Keras API.[6] Finally, the inverse standardization operation is applied to the CNN's output to get

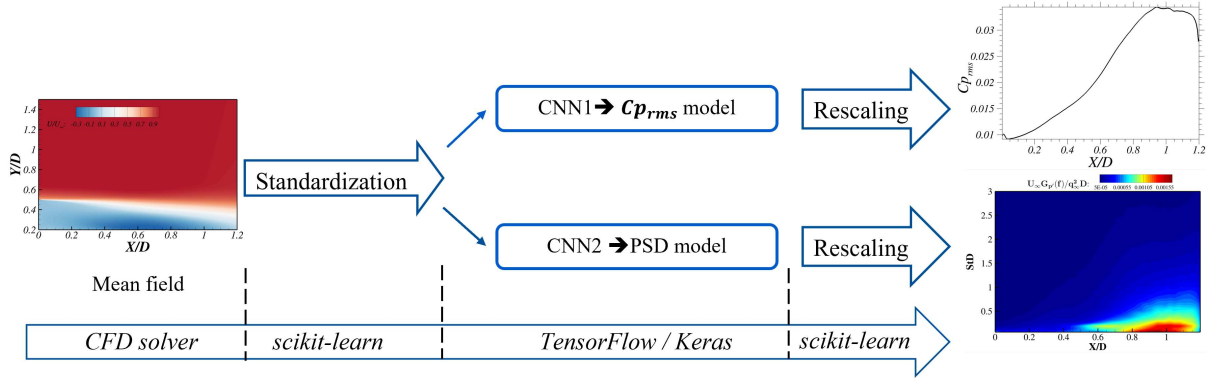the predicted physical quantity.

Figure 6: Schematic representation of the prediction process.

3.2 Construction of the datasets

The studied configurations being axisymmetric, the mean flow variables are averaged along the azimuthal direction. The input flow fields are therefore two-dimensional.

3.2.1 Input datasets

The choice of the input flow features was based on the study of existing analytical models.[2,3,16,29] These models solve the Poisson equation governing pressure fluctuations, and relate the wall-pressure spectrum to mean flow variables such as velocity, pressure and their gradients, coupled with modelled turbulence statistics.

Our data-driven approach is inspired from these physical approaches. Wall-normal profiles of the aforementioned mean flow variables form the input datasets (for training or testing depending on the configuration). The studied flows being compressible (transonic regime), conservative variables ρU and ρV are considered instead of U and V, with ρ the density, U and V standing for the mean streamwise and radial velocity components, respectively. Finally, input features are normalized using geometry and free stream characteristics in a purpose of generalization. The input variable along with their normalization factors are listed in table 1.

Table 1: Nondimensional flow features used as input for the neural networks.

Input	Raw input	Normalization factor
Streamwise velocity	ρU	$\rho_\infty U_\infty$
Wall-normal velocity	ρV	$\rho_\infty U_\infty$
Streamwise velocity gradient in the streamwise direction	$\frac{\partial \rho U}{\partial x}$	$\frac{\rho_\infty U_\infty}{D}$
Normal velocity gradient in the streamwise direction	$\frac{\partial \rho V}{\partial x}$	$\frac{\rho_\infty U_\infty}{D}$
Streamwise velocity gradient in the normal direction	$\frac{\partial \rho U}{\partial y}$	$\frac{\rho_\infty U_\infty}{D}$
Normal velocity gradient in the normal direction	$\frac{\partial \rho V}{\partial y}$	$\frac{\rho_\infty U_\infty}{D}$
Static pressure	P	q_∞
Pressure gradient in the streamwise direction	$\frac{\partial P}{\partial x}$	$\frac{q_\infty}{D}$

3.2.2 Output datasets

Output data are only used during the training process. During this stage, weights and biases of the neural networks are updated to fit the predicted output to the corresponding reference output data.

The first output dataset includes the value of Cp_{rms} for each streamwise location of the domain of interest, obtained by averaging along the azimuthal direction. For each of the 171 streamwise numerical sensors distributed along the S3Ch afterbody, the power spectra dataset is constituted by 67 values (as will be seen in figure 9) of the common logarithm of dimensionless PSD ($10\log_{10}(U_\infty G'_p(f)/Dq_\infty^2)$), covering a wide frequency band. Moreover, the PSD has

been willingly computed with a low frequency resolution of 152 Hz to get a relatively smooth spectrum in the training process. Finally, the PSD values computed from the 240 azimuthal coordinates were averaged in the homogeneous direction.

3.3 Basics on Artificial Neural Networks (ANNs)

An artificial neural network is formed by successive layers of artificial neurons (hidden layers) between an input and an output layer. An artificial neuron represents the most basic computational unit. A schematic representation is displayed in figure 7. The neuron performs a weighted sum of the inputs x_i with a given bias b. An activation function f, (often non linear) is applied to the result. The neuron output y equals:

$$y = f(\sum_{i=1}^{N} w_i x_i + b) \tag{1}$$

The number of layers and the number of neurons N in each layer as well as the chosen type of activation function are called hyperparameters and need to be carefully chosen to get optimal training. Weights w_i and bias b are determined during the training process through a back propagation algorithm. This optimization algorithm minimizes a loss function $J(\mathbf{y}, \overline{\mathbf{y}})$ where $\mathbf{y}$ is the output vector of the network and $\overline{\mathbf{y}}$ the expected output given by the training output dataset.
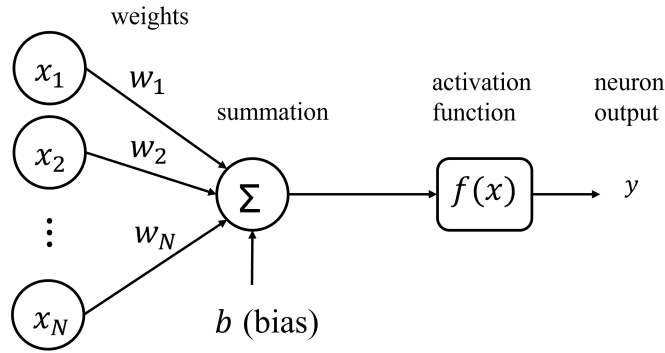

Figure 7: Neuron in a hidden layer of an artificial neural network

3.4 Basics on Convolutional Neural Networks (CNNs)

Convolutional Neural Networks are a special type of ANNs. We selected this kind of network due to their ability to extract spatial features from input data.[31,37,38] They are made of three different types of hidden layers: Convolutional layers, pooling layers and fully-connected (dense) layers. In the present study we used 1D convolutional layers. In such type of layers, the weights introduced in figure 7 for basic artificial neurons are replaced by convolutional kernels. The kernel (also called filter) $\mathbf{k}$ shifts along the data, performing a matrix multiplication operation between the filter $\mathbf{k}$ and the portion of the data over which the kernel is hovering. The analogous relation of equation 1 for a convolutional layer is:

$$y = f(\mathbf{k} * \mathbf{x} + b) \tag{2}$$

where * denotes the convolution operation. The convolution process is illustrated in figure 8 on input data of height H and depth D and a kernel of size K moving with a stride equal to 1. The output of this convolutional layer is a matrix of size $(H - K + 1) \times L$ with L the number of kernels (1 in this example).

A convolutional layer is followed by a so-called pooling layer that aims at reducing the dimension of data while preserving the detected features. It allows to avoid overfitting and reduce the number of parameters in the network. Overfitting means that the model performs well on the training set, but poorly on unknown data. The chosen pooling operation is the maximum pooling. This operation consists in selecting the maximum value in the pooling window that shifts along the data. It is also illustrated in figure 8. Finally, the fully connected layer connects each neuron to all nodes in the next layer through equation 1.
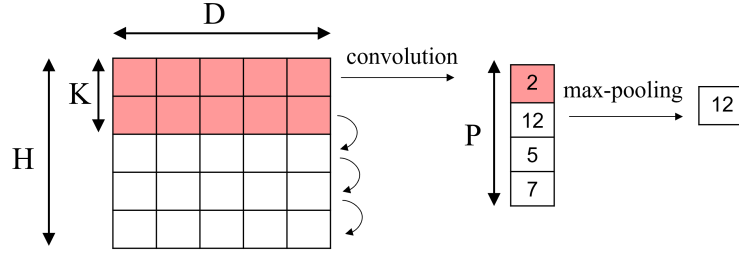
Figure 8: Schematic diagram of the convolution and max-pooling processes used in the architecture detailed in figure 9 with 1 kernel.

3.5 CNNs architectures and training

The architecture of both CNNs designed in this study is detailed in figure 9. For a given streamwise position in the flow, the input is a matrix of size $D \times H = 8 \times 105$. D refers to the 8 input flow variables listed table 1, and H is the number of points in the wall-normal flow profile. In figure 9, the ith feature after the preprocessing step (standardization of the dataset detailed in section 3.1) is referred to as e_i. Conversely, s_i refers to as the ith component of the output vector before applying the inverse standardization operation.

Due to the preprocessing procedure, any data provided as input to the network will have zero mean and unit standard deviation, hence the same statistical distribution. As a consequence, if the testing case has different statistical properties, the network will not be able to take it into account. As a consequence, the model is expected to predict the relative evolution of the output quantities (shape of the curve $Cp_{rms}(X/D)$ for example), or the precise location of the pressure fluctuations maximum, but not the correct levels of the physical quantities of interest. However, as shown in section 4, a physical scaling based on free stream parameters can be applied to retrieve accurate magnitudes of pressure fluctuations. As for the networks architecture, both CNNs consist in three series of convolutional/max-pooling layers. The last hidden layer is a fully connected layer with a linear activation function. The first CNN (referred to as CNN1) outputs a scalar corresponding (after inverse standardization) to the RMS pressure coefficient at the considered streamwise position. The output of the second CNN (CNN 2) is a vector of size 67 containing the logarithm of dimensionless PSD values. Each convolutional layer uses a rectified-linear-unit (ReLU(x) = max(0,x)) activation function while fully-connected layers use linear activation functions. A grid search with a cross-validation procedure is used to select the optimal hyperparameters.

The training was performed using Adam optimizer[18] (stochastic gradient descent) with a batch size of 96 samples. L2 regularization and early stopping were used to prevent overfitting.[14] To overcome the latter issue, a common practice is to split the dataset into training and validation set. The validation set is used to compute the validation loss during training. Overfitting occurs when the training loss decreases but the validation loss starts increasing. To prevent this undesirable effect, early stopping allows to interrupt the training process automatically when the validation loss stops to decrease. Besides, L2 regularization penalizes excessive weight values using the L2 norm. The mean-squared error was selected as a loss function:

$$J(\mathbf{s}, \bar{\mathbf{s}}) = \frac{1}{n} \sum_{i=1}^{n} |\mathbf{s_i} - \bar{\mathbf{s_i}}|^2 + \lambda \|\mathbf{w}\|_2 \tag{3}$$

with n the size of the output layer (respectively 1 and 67 for the Cp_{rms} and PSD models), $\mathbf{s}$ and $\bar{\mathbf{s}}$ respectively the predicted and true n-dimensional vectors (before inverse standardization) and λ the regularization parameter. CNN 1 and CNN 2 contain respectively a total of 10641 and 16047 trainable parameters (weights and biases). Training time was 243 s, including 9944 epochs for CNN 1, and 248 s with 9865 epochs for CNN 2. An epoch is defined as one cycle of the training algorithm through the full training set.

4. Results

4.1 Training

The training process is illustrated in figure 10. The evolution of the training and validation loss functions with training epochs is displayed for both trained CNNs. Thanks to the early stopping criterion, it can be seen that training ends when the validation loss stops decreasing.

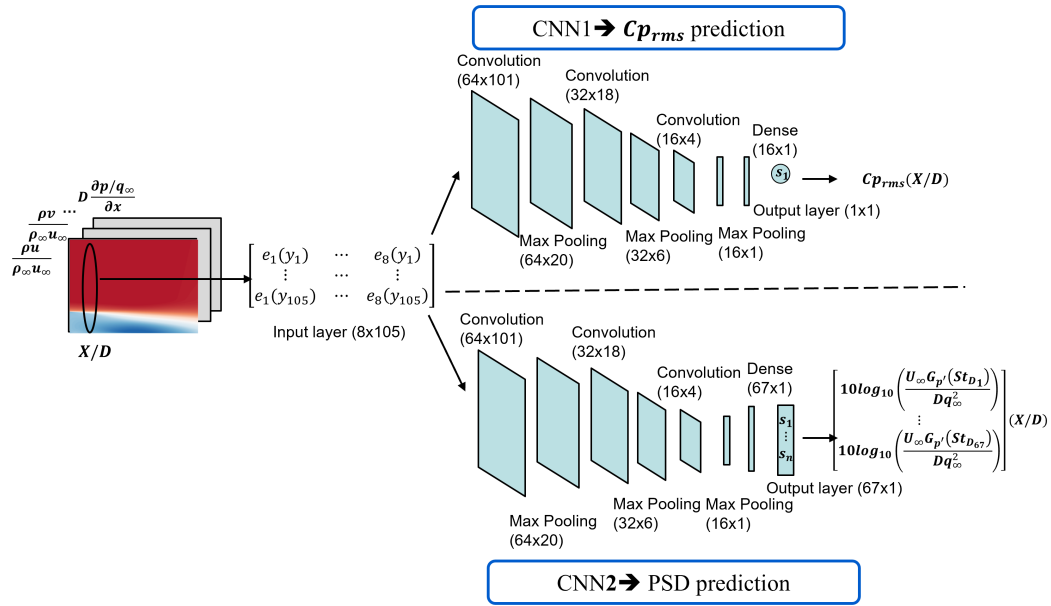PREDICTION OF WALL-PRESSURE FLUCTUATIONS FOR SPACE LAUNCHERS USING CNN

Figure 9: Architectures of the two convolutional neural networks (CNN1 and CNN2) used for the prediction of Cp_{rms} and the pressure spectra.
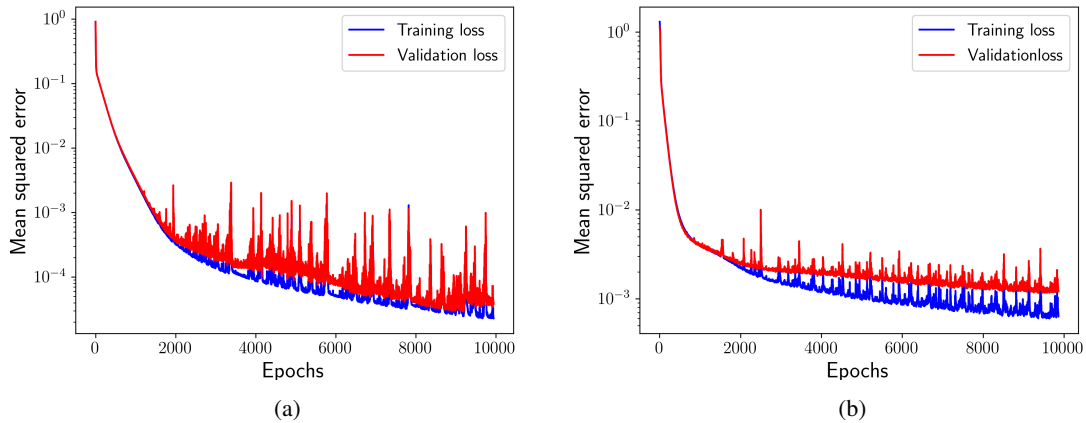

Figure 10: Evolution of the training and validation loss functions during training of CNN 1 (Fig.10a) and CNN 2 (Fig. 10b).

Once training is over and before assessing the generalisation capability of the networks, it is checked that the present models perform well on the training case. The evolution of Cp_{rms} and pressure spectra at 9 streamwise locations along the wall are plotted in figures 11 and 12, along with the reference ZDES results used for training. One can see that curves are almost entirely superposed, proving that training succeeded.

4.2 Prediction on the NASA Model 11 test case

The trained models were applied to the testing dataset corresponding to the separating/reattaching zone of the NASA model 11 launch vehicle (referred to as M11 in the following). The Cp_{rms} curves obtained with CNN 1 are first discussed in section 4.2.1. Finally, pressure spectra resulting from CNN 2 are presented in section 4.2.2.
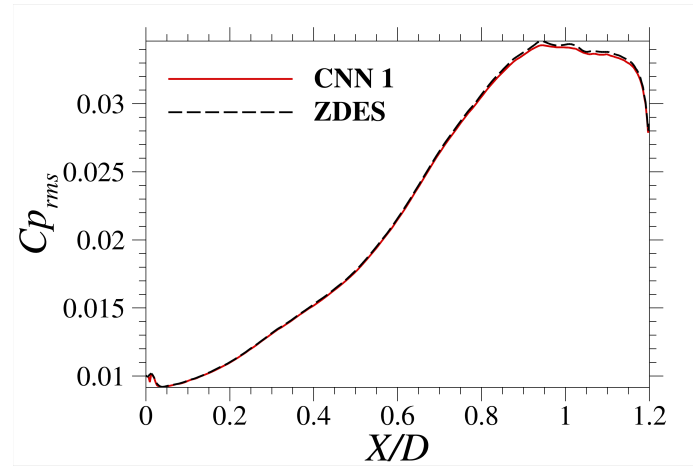
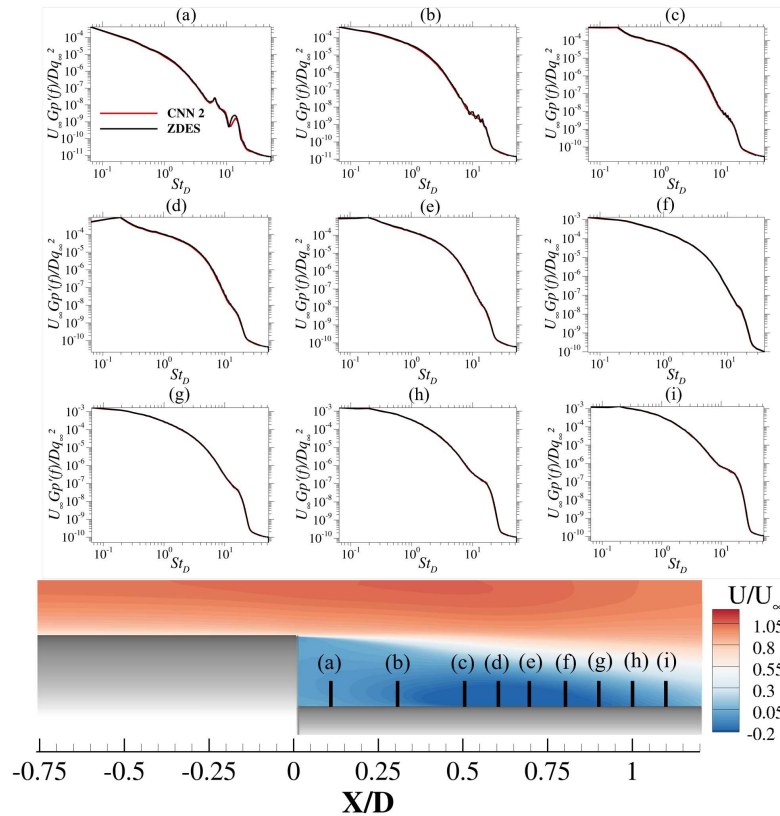Figure 11: True and learned evolutions of the fluctuating pressure coefficient for the training case.

Figure 12: True and learned spectra for the training case at 9 streamwise positions.

4.2.1 Cp_{rms} **prediction**

As explained in section 3.5, the CNN's output lies in the range [-1 , 1] and needs to be scaled by applying the inverse standardization operation (mutliplying by the standard deviation and adding the mean of training output data). The resulting predicted Cp_{rms} is plotted in figure 13 (dotted line). As expected, our model is able to predict the evolution of this quantity along the streamwise direction, and to accurately locate the position of maximum pressure fluctuations level. However, the levels of pressure fluctuations are underpredicted as their mean value and standard deviation are imposed by the training data. This is illustrated in the same figure. CNN1's output is scaled using the mean and standard deviation values computed from the testing case (continuous red line). For a given configuration, these values are supposed to be unknown, but are used here for the purpose of illutration. One can see that the correct magnitudes are retrieved. It is of major importance to note that this standardization procedure only affects the overall levels of the

9

Cp_{rms} curve. The position of the RMS-pressure peak and the general evolution of this quantity are well predicted by the neural network.
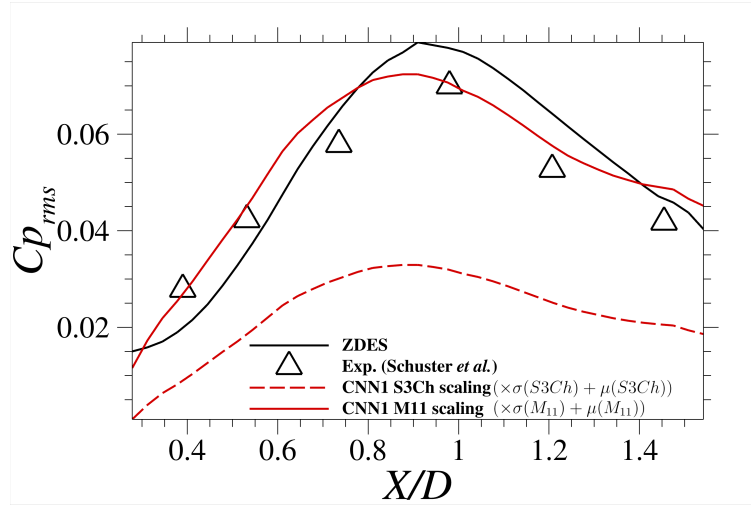

Figure 13: Predicted evolution of the fluctuating pressure coefficient along the wall using training case (red plain line) and testing case (red dotted line) for inverse standardization.

The correct levels of pressure fluctuations being a-priori unknown for a given application case, a scaling procedure is necessary to retrieve accurate output magnitudes. Robertson[25] experimentally studied wall-pressure fluctuations around axisymmetric cone-cylinder, cone-cylinder-flare and cone-cylinder-boattail configurations. In regions of separating/reattaching flows, this author proposed the following empirical correlation $\mathscr{C}$ for the root-mean-square pressure p_{rms}:

$$\mathscr{C} = \frac{0.045 q_\infty}{1 + M_\infty^2} \tag{4}$$

Therefore, the following scaling factor will be applied to relate pressure fluctuations magnitudes:

$$\frac{q_{\infty|M11}\left(1 + M_{\infty|S3Ch}^2\right)}{q_{\infty|S3Ch}\left(1 + M_{\infty|M11}^2\right)} \tag{5}$$

Figure 14 shows the Cp_{rms} curve obtained after applying this scaling factor (blue line). One can see that the corrected levels of pressure fluctuations are in fair agreement with ZDES and experimental results. The shape of the curve also evidences the success of our trained model to predict the evolution of Cp_{rms} along the wall. In particular, the zone of high pressure fluctuations is accurately located.

The influence of the turbulence model and the type of simulation used to produce the input data through the CFD solver is then investigated. As the trained CNN only needs mean flow profiles to predict fluctuating quantities, it would be beneficial in terms of computational cost to build the input dataset for a given application case using RANS simulations instead of ZDES ones. However, RANS models are usually less accurate in predicting the present type of flows, namely separated flows.[4, 17] The Cp_{rms} predictions using the same model (CNN 1) applied using either ZDES, RANS Spalart-Allmaras or RANS Spalart-Allmaras with rotation correction (SA-R) mean flow fields as input are plotted in figure 15. Results are rescaled using expression 5. It can be observed that the three curves are quite close. The location of the maximum is slightly shifted from one curve to another. This could be related to small discrepancies in the position of the mean reattachment point predicted by the different simulations. One can note from figure 15 that our data-driven model is able to make a fair prediction of the wall-pressure fluctuations from a RANS mean flow field as input. This represents an outstanding gain in term of computational resources and time compared to the realisation of a full unsteady numerical simulation which can take from a few weeks to several months.

4.2.2 Wall-pressure spectra prediction

The trained model CNN 2 is then applied to predict dimensionless single-point wall-pressure spectra for the M11 configuration. Similarly to the Cp_{rms} curves, the power spectral densities (PSD) resulting from the CNN prediction need to be rescaled in order to be compared to the reference ZDES data. We assumed in section 4.2.1 that the magnitude of pressure fluctuations is proportional to $\frac{q_\infty}{1+M_\infty^2}$. In the same spirit as in Panda et al.,[23] it is then assumed that the power
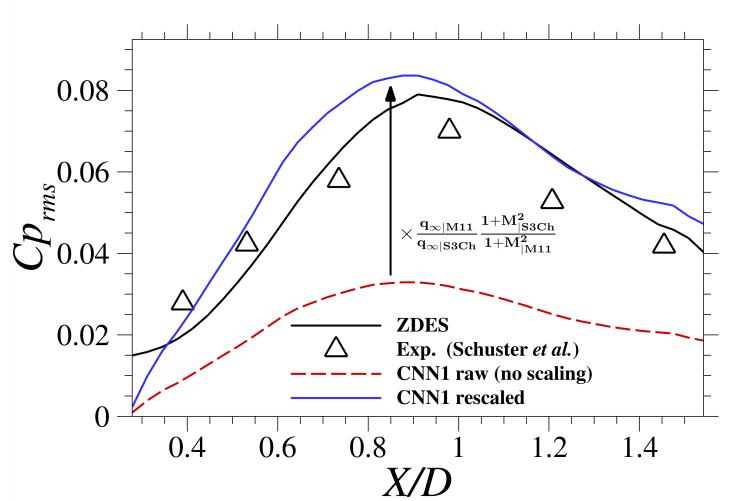
Figure 14: Predicted evolution of the fluctuating pressure coefficient along the wall. Comparison of raw data (red dotted line) and rescaled data (solid blue line) using a scaling factor adapted from Robertson.[25]
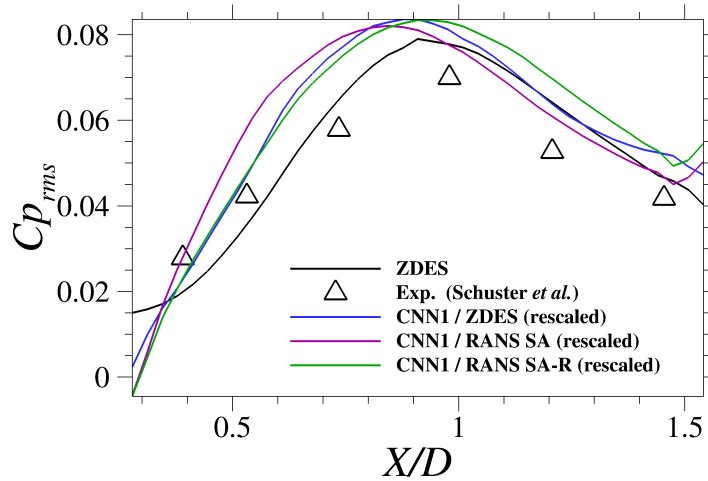

Figure 15: Rescaled predicted evolution of the fluctuating pressure coefficient along the wall using ZDES, RANS SA and RANS SAR flow fields as input.

spectral density of pressure fluctuations is proportional to $\left(\frac{q_\infty}{1+M_\infty^2}\right)^2$. The applied scaling factor is therefore the squared value of expression 5.

Moreover, the Strouhal number needs to be rescaled as well. Indeed, predicted PSD values correspond to the same Strouhal numbers as in the training case. These values are computed using reference diameter and free stream velocitiy. It can be seen in figure 16 that predicted raw spectra are slightly shifted towards the low frequencies with respect to the reference ZDES spectra. Applying the scaling factor given in equation 6 allows to bridge this gap (see blue line in figure 16). Finally, the PSD scaling factor is applied to the dimensionless PSD to get the corrected predicted spectrum (green line) at streamwise position $X/D = 1.1$, which corresponds to the mean reattachment point. This spectrum is superposed to the ZDES spectrum in a wide frequency range ($St_D \in [0.5, 40]$). In the low frequency range, the CNN overpredicts the PSD. However, due to the limited duration of the simulation (300 ms), few points are available to train the model in this frequency range. In the high frequency range, a sudden drop of the predicted PSD is observed after $St_D = 20$, and no data is plotted after $St_D = 50$. Indeed, as stated in section 2.1, training data are acquired at a sampling frequency of 250 kHz. The CNN is therefore trained with frequencies less than 125 kHz according to the Nyquist-Shnannon criterion, corresponding to Strouhal numbers less than 50. Hence, no PSD value can be predicted for higher Strouhal numbers.

$$St_{D|scaled} = St_D * \frac{D_{M_{11}} U_{\infty|S3Ch}}{D_{S3Ch} U_{\infty|M_{11}}} \qquad (6)$$
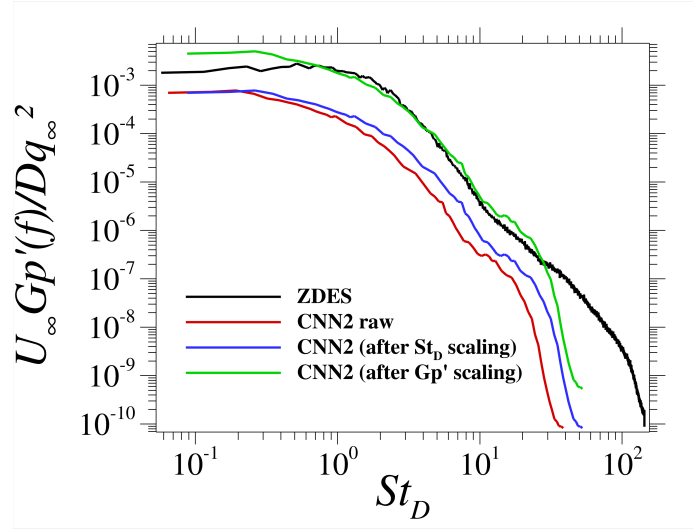

Figure 16: Predicted wall-pressure spectrum at $X/D = 1.1$ using raw CNN output, scaling of the Strouhal number and scaling of both Strouhal number and dimensionless power spectral density.

Rescaled predicted spectra using ZDES, RANS SA and RANS SA-R mean flow fields at different streamwise positions are plotted in figure 17. A similar trend is observed: predictions are few sensitive to the underlying turbulence model. They fit well the ZDES spectra in the medium frequency range and overpredict the PSD in the low frequency range. The PSD also drops abruptly for high Strouhal numbers. Finally, one can note that the quality of predictions is decreased compared to the one obtained with a ZDES time-averaged flow at the beginning (position (a)) and at the end (position (i)) of the domain. Indeed, the flow field at both of these streamwise positions is quite different from the S3Ch training case. In the latter case, the flow separation is caused by a sudden expansion. In the application case, an inclined wall follows the separation point. One can assume that this geometric difference has a significant influence on the mean flow field at the beginning of the working domain, impacting the CNN's prediction. As for point (i) in figure 17, it is located quite far from the reattachment point, while the training domain ends immediately after the reattachment. The CNN was therefore not trained in this area of the flow.

Finally, figure 18 displays the rescaled predicted dimensionless PSD map (left) compared to the reference PSD map resulting from the ZDES simulation (right). As it was shown in figures 16 and 17, levels of dimensionless PSD are overestimated for low Strouhal numbers. As a consequence, figure 18(a) displays a larger zone of high energy fluctuations (zone 1 of width L), that characterizes the oscillation of the reattachment point around its mean streamwise position.[19] This high level of fluctuations at low frequencies originates from the impingement of turbulent structures on the wall and from the flapping motion of the shear layer. However, this region is accurately located and centered around $X/D \simeq 0.85$ by the CNN. At the end of the domain, the CNN still predicts overestimated pressure fluctuations levels at low frequencies compared to those obtained with the reference ZDES simulation. As stated previously, this could be explained by the fact that the CNN was not trained for this region of the flow. The frequency distribution of the energy of pressure fluctuations is similar in both cases. Characteristics zones of medium and low intensity fluctuations (zones 2 and 3) have roughly the same size along the Strouhal number axis. One can suggest that these high-frequency fluctuations reveal the wall signature originating from the growing vortices in the shear layer, as observed in Spazzini et al.[30] and Deck and Thorigny.[12]

5. Conclusion and perspectives

In this work, models based on Convolutional Neural Networks have been developed to predict the wall-pressure fluctuations for a separating/reattaching transonic flow around a generic space launcher. Training and testing cases were computed using ZDES. Our models successfully identify regions of high pressure fluctuations and predict the relative evolution of the fluctuating pressure coefficient and the power spectra along the wall. A scaling method based on an experimental correlation was proposed to retrieve accurate magnitudes of pressure fluctuations for a given application
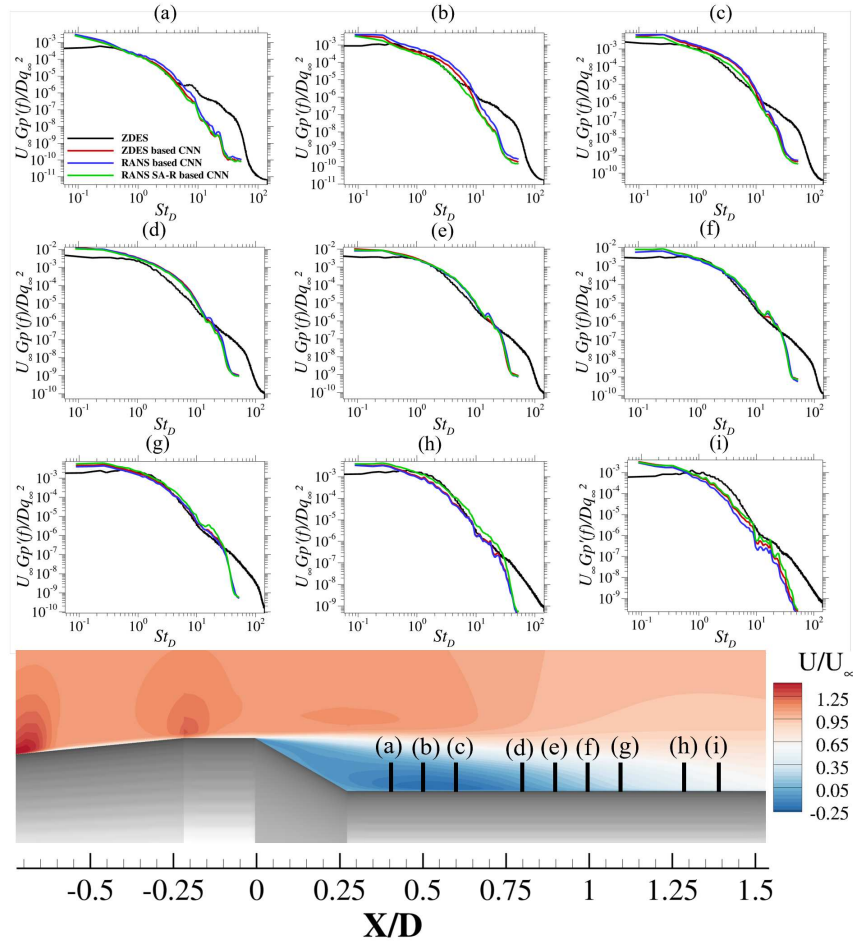
Figure 17: Predicted and rescaled wall-pressure spectra at different streamwise positions using and ZDES, RANS SA and RANS SA-R flow fields as input
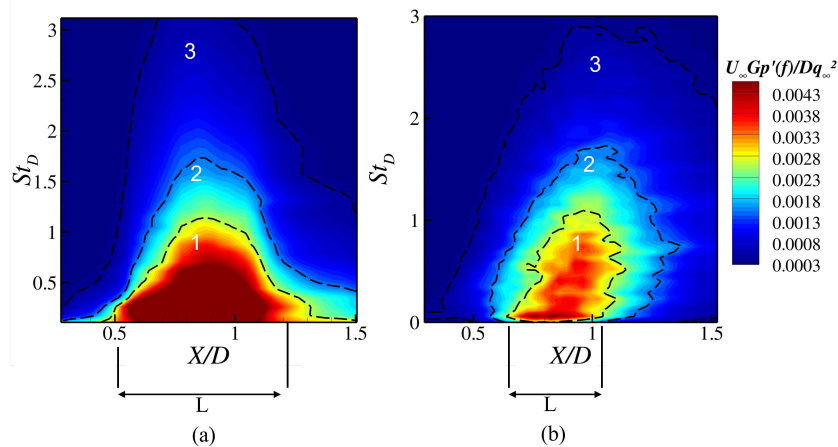

Figure 18: Predicted and rescaled (left) and ZDES dimensionless power spectral density (PSD) maps of the fluctuating pressure

case with different free stream properties. We also demonstrated the feasibility to use RANS simulations as input, allowing a drastic reduction of the computational cost.

In future works, our models will be applied and evaluated on various configurations. It could also be extended to different types of flows. Finally, a sensitivity study to the input variables will be conducted, along with efforts to understand the mechanisms involved in the prediction process by the CNNs.

6. Acknowledgments

References

[1] A. Agarwal, P. Barham, E. Brevdo, Z. Chen, C. Citro, G. S. Corrado, A. Davis, J. Dean, M. Devin, S. Ghemawat, I. Goodfellow, A. Harp, G. Irving, M. Isard, Y. Jia, R. Jozefowicz, L. Kaiser, M. Kudlur, J. Levenberg, D. Man, R. Monga, S. Moore, D. Murray, C. Olah, M. Schuster, J. Shlens, B. Steiner, I. Sutskever, K. Talwar, P. Tucker, V. Vanhoucke, V. Vasudevan, F. Vi, O. Vinyals, P. Warden, M. Wattenberg, M. Wicke, Y. Yu, and X. Zheng. TensorFlow: Large-Scale Machine Learning on Heterogeneous Distributed Systems. 2015.

[2] B. Aupoix. Extension of Lysak's approach to evaluate the wall pressure spectrum for boundary layer flows. *Flow, Turbulence and Combustion*, 94(1):63–78, 2015.

[3] F. Bertagnolio, A. Fischer, and W. Jun Zhu. Tuning of turbulent boundary layer anisotropy for improved surface pressure and trailing-edge noise modeling. *Journal of Sound and Vibration*, 333(3):991–1010, 2014.

[4] M. Breuer, N. Jovičić, and K. Mazaev. Comparison of DES, RANS and LES for the separated flow around a flat plate at high incidence. *International Journal for Numerical Methods in Fluids*, 41(4):357–388, 2003.

[5] D. M. Chase. Modeling the wavevector-frequency spectrum of turbulent boundary layer wall pressure. *Journal of Sound and Vibration*, 70(1):29–67, 1980.

[6] F. Chollet. Keras, 2015.

[7] C. F. Coe and J. B. Nute. Steady and fluctuating pressures at transonic speeds on hammerhead launch vehicles. Technical Report NASA-TM-X-778, 1962.

[8] H. A. Jr. Cole, A. L. Erickson, and A. G. Rainey. Buffeting during atmospheric ascent. Technical Report NASA SP-8001, NASA, 1964.

[9] G. M. Corcos. Resolution of Pressure in Turbulence. *The Journal of the Acoustical Society of America*, 35(2):192–199, 1963.

[10] S. Deck. Recent improvements in the Zonal Detached Eddy Simulation (ZDES) formulation. *Theoretical and Computational Fluid Dynamics*, 26(6):523–550, 2012.

[11] S. Deck and N. Renard. Towards an enhanced protection of attached boundary layers in hybrid RANS/LES methods. *Journal of Computational Physics*, 400, 2020.

[12] S. Deck and P. Thorigny. Unsteadiness of an axisymmetric separating-reattaching flow: Numerical investigation. *Physics of Fluids*, 19(6), 2007.

[13] D. Deprés, P. Reijasse, and J. P. Dussauge. Analysis of unsteadiness in afterbody transonic flows. *AIAA Journal*, 42(12):2541–2550, 2004.

[14] I. Goodfellow, Y. Bengio, and A. Courville. Deep learning. *Genetic Programming and Evolvable Machines*, 19(1):305–307, 2018.

[15] M. Goody. Empirical spectral model of surface pressure fluctuations. *AIAA Journal*, 42(9):1788–1794, 2004.

[16] G. Grasso, P. Jaiswal, H. Wu, S. Moreau, and M. Roger. Analytical models of the wall-pressure spectrum under a turbulent boundary layer with adverse pressure gradient. *Journal of Fluid Mechanics*, 877:1007–1062, 2019.

[17] G. Iaccarino, A. Ooi, P. A. Durbin, and M. Behnia. Reynolds averaged simulation of unsteady separated flow. *International Journal of Heat and Fluid Flow*, 24(2):147–156, 2003.

[18] D. P. Kingma and J. L. Ba. Adam: A method for stochastic optimization. *3rd International Conference on Learning Representations, ICLR 2015 - Conference Track Proceedings*, pages 1–15, 2015.

[19] Y. Liu, G. Wang, H. Zhu, and Z. Ye. Numerical analysis of transonic buffet flow around a hammerhead payload fairing. *Aerospace Science and Technology*, 84:604–619, 2019.

[20] P. D. Lysak. Modeling the wall pressure spectrum in turbulent pipe flows. *Journal of Fluids Engineering, Transactions of the ASME*, 128(2):216–222, 2006.

[21] P. Meliga and P. Reijasse. Unsteady transonic flow behind an axisymmetric afterbody with two boosters. In *25th AIAA Applied Aerodynamics Conference*, June 2007.

[22] R. Pain, P. É. Weiss, S. Deck, and J. C. Robinet. Large scale dynamics of a high Reynolds number axisymmetric separating/reattaching flow. *Physics of Fluids*, 31(12), 2019.

[23] J. Panda, T. J. Garbeff, N. J. Burnside, and J. C. Ross. Unsteady pressure fluctuations measured on a hammerhead space vehicle and comparison with Coe and Nute's 1962 data. *International Journal of Aeroacoustics*, 17(1-2):70–87, 2018.

[24] J. Panda, N. H. Roozeboom, and J. C. Ross. Wavenumber-frequency spectra on a launch vehicle model measured via unsteady pressure-sensitive paint. *AIAA Journal*, 57(5):1801–1817, 2019.

[25] J.E Robertson. Prediction of in-flight fluctuating pressure environments including protuberance induced flow. Technical Report WR-71-10, NASA-CR-119941, Wyle Laboratories Research Staff, Huntsville, 1971.

[26] D. M Schuster, J. Panda, J. C Ross, N. H. Roozeboom, N. J. Burnside, C. L. Ngo, M. Sellers, and J. M. Powell. Investigation of Unsteady Pressure-Sensitive Paint (uPSP) and a Dynamic Loads Balance to Predict Launch Vehicle Buffet Environments. Technical Report NSA/TM-2016-219352, 2016.

[27] M. Shanker, M. Y. Hu, and M. S. Hung. Effect of Data Standardization on Neural Network Training. *The International Journal of Management and Science*, 24(4):385–397, 1996.

[28] F. Simon, S. Deck, P. Guillen, P. Sagaut, and A. Merlen. Numerical simulation of the compressible mixing layer past an axisymmetric trailing edge. *Journal of Fluid Mechanics*, 591:215–253, 2007.

[29] M. Slama, C. Leblond, and P. Sagaut. A Kriging-based elliptic extended anisotropic model for the turbulent boundary layer wall pressure spectrum. *Journal of Fluid Mechanics*, 840:25–55, 2018.

[30] P. G. Spazzini, G. Iuso, M. Onorato, N. Zurlo, and G. M. Di Cicca. Unsteady behavior of back-facing step flow. *Experiments in Fluids*, 30(5):551–561, 2001.

[31] C. M. Ströfer, J. Wu, H. Xiao, and E Paterson. Data-driven, physics-based feature extraction from fluid flow fields. *arXiv*, 2018.

[32] G. Varoquaux, L. Buitinck, G. Louppe, O. Grisel, F. Pedregosa, and A. Mueller. Scikit-learn: Machine Learning in Python. *Journal of Machine Learning Research*, 12:2825–2830, 2011.

[33] Gang Wang, Quanzheng Li, and Yi Liu. IDDES method based on differential Reynolds-stress model and its application in bluff body turbulent flows. *Aerospace Science and Technology*, 119:107207, 2021.

[34] P. É. Weiss. ZDES of an Ariane 6 PPH configuration with incidence angle using Zonal Immersed Boundary Conditions. In *European Conference for Aeronautics and Space Sciences.*, 2019.

[35] P. É. Weiss and S. Deck. Numerical Investigation of the Robustness of an Axisymmetric Separating/Reattaching Flow to an External Perturbation Using ZDES. *Flow, Turbulence and Combustion*, 91(3):697–715, 2013.

[36] P. É. Weiss, S. Deck, J.C. Robinet, and P. Sagaut. On the dynamics of axisymmetric turbulent separating/reattaching flows. *Physics of Fluids*, 21(7), 2009.

[37] S. Ye, Z. Zhang, X. Song, Y. Wang, Y. Chen, and C. Huang. A flow feature detection method for modeling pressure distribution around a cylinder in non-uniform flows by using a convolutional neural network. *Scientific Reports*, 10(1):1–10, 2020.

[38] Y. Yin, P. Yang, Y. Zhang, H. Chen, and S. Fu. Feature selection and processing of turbulence modeling based on an artificial neural network. *Physics of Fluids*, 32(10), 2020.